

Article

Influences of Modified Sm_2O_3 on Thermal Stability, Mechanical and Neutron Shielding Properties of Aminophenol Trifunctional Epoxy Resin

Hongqing Wang^{1,2,*}, Qunying Huang² and Yutao Zhai²¹ Institutes of Physics Science and Information Technology, Anhui University, Hefei 230601, China² Institute of Nuclear Energy Safety Technology, Hefei Institutes of Physical Science, Chinese Academy of Sciences, Hefei 230031, China; qunying.huang@inest.cas.cn (Q.H.); yutao.zhai@inest.cas.cn (Y.Z.)

* Correspondence: whq1997@mail.ustc.edu.cn

Abstract: The requirements regarding the weight and capacity reduction of neutron shielding materials have become an urgent issue for advanced nuclear facilities and plants. An epoxy-based neutron shielding material with high-temperature stability and good neutron irradiation resistance was designed in this paper to solve the above issue. Aminophenol trifunctional epoxy resin (AFG-90H) was compounded with samarium oxide (Sm_2O_3) by means of an ultrasonic-assisted method and the compatibility of Sm_2O_3 with the AFG-90H matrix was improved by 3-aminopropyltriethoxysilane (APTES) surface modification. Fabricated Sm_2O_3 -APTES/AFG-90H composites exhibited improved thermal stability, glass transition temperature and Young's modulus with increased Sm_2O_3 -APTES content. Neutronics calculation results show that the neutron permeability of 2 mm-thick 30 wt% Sm_2O_3 -APTES/AFG-90H was 98.9% higher than that of the AFG-90H matrix under the irradiation of the thermal neutron source. The results show that the proper addition range of Sm_2O_3 -APTES is between 20% and 25%. The Sm_2O_3 -APTES/AFG-90H composite is a promising neutron shielding material for advanced nuclear system.

Keywords: aminophenol trifunctional epoxy resin; samarium oxide; thermal energy neutron source; thermal stability; mechanical property



Citation: Wang, H.; Huang, Q.; Zhai, Y. Influences of Modified Sm_2O_3 on Thermal Stability, Mechanical and Neutron Shielding Properties of Aminophenol Trifunctional Epoxy Resin. *Polymers* **2022**, *14*, 638. <https://doi.org/10.3390/polym14030638>

Academic Editor: Albertino Arterio

Received: 8 January 2022

Accepted: 31 January 2022

Published: 8 February 2022

Publisher's Note: MDPI stays neutral with regard to jurisdictional claims in published maps and institutional affiliations.



Copyright: © 2022 by the authors. Licensee MDPI, Basel, Switzerland. This article is an open access article distributed under the terms and conditions of the Creative Commons Attribution (CC BY) license (<https://creativecommons.org/licenses/by/4.0/>).

1. Introduction

Neutron radiation exists not only in nuclear reactors, but also in various industrial, aviation and radiotherapy fields [1–4]. Uncharged neutrons can easily penetrate human tissues and cause ionization, which seriously threatens human health. Moreover, neutron radiation can also have a fatal negative impact on the service lifetime of electronic components and the environment [5]. As a result, the R&D on radiation protection materials is widely performed in the nuclear-related fields, including neutron shielding materials.

Neutrons shielding processes include two steps: moderating and absorbing [6,7]. High-energy neutrons (>1 MeV) first undergo inelastic scattering with substances with high atomic numbers and then lose energy, or undergo multiple elastic scattering with materials rich in hydrogen and then reduce energy to thermal neutrons (~eV). Thermal neutrons are easily captured or absorbed by elements with high neutron absorption cross-sections [8]. As described above, traditional shielding materials are roughly divided into metal, concrete and polymer materials according to their compositions. At present, the commercial metal-based shielding materials mainly include boron-containing stainless steel. Divya et al. pointed out that the serious problem with boron-containing stainless steels is the formation of low-melting point eutectics, makes this class of steel susceptible to heat cracking [9]. Maurya et al. studied the influence of various processing parameters on the strength, hardness and strain to failure of B_4C particle reinforced Al-alloy matrix composites. When the content of B_4C exceeded 10%, the strength and strain of $\text{B}_4\text{C}/\text{Al}$ to failure decreased

due to particle agglomeration [10]. In addition, the commonly used concrete shielding materials mainly include boron-containing concrete and cement composites. Chidiac et al. studied the heat evolution, compressive strength and neutron shielding capabilities of hydrated mixes containing 0, 25, 50 and 75 wt% of B_4C . The results show that a concrete mix containing up to 50 wt% B_4C was found to be beneficial to the development of concrete properties and to effective neutron shielding [11]. Sevim et al. studied the strength and fresh properties of borogypsum concrete. They showed that an addition of 4 wt% of boron sludge could reduce the 90-day compressive strength of concrete by 65 wt% [12]. However, the requirements regarding the above materials in nuclear power stations and facilities are a large engineering amount and a heavy weight [13]. There are limitations in transportation and small modular manufacturing. Currently, the fourth-generation advanced nuclear power system puts forward the target of “integration of structure and function” with the demand for weight and capacity reduction. Therefore, developing new neutron shielding materials with outstanding properties has become one of the promoted ways to satisfy the requirements of neutron protection.

Blending hydrogen-rich polymer matrix with high neutron cross-section absorbing elements can integrate neutron moderation and absorption. So, these materials are expected to become alternative materials for metals and concrete in nuclear facilities, such as polyethylene (PE) [14,15], high-density polyethylene (HDPE) [16,17], epoxy resin (EP) [18,19], ethylene propylene diene monomer (EPDM) [20] and polyimide (PI) [21,22], etc. Although PE and EPDM matrix have good processability, they have low thermal stability and it is difficult to use them at a temperature higher than 100 °C for a long time. PI has high temperature stability and good mechanical properties. Wu et al. studied composites based on carbon fiber-reinforced carborane-containing polyimides. The results show that the thermoset polyimide matrixes exhibited high thermal stability with $T_5 > 800$ °C both in nitrogen and air environments [23]. However, the synthesis process of PI is more complex than other polymers and it is mostly used in membrane products. It is difficult to break through to large-scale preparation. Among the above polymers, EP has good chemical stability and structure stability. Jiang et al. blended B_4C particles with AFG-90H to develop a new type of AFG-90H epoxy resin-based composite, and the results show good neutron shielding and mechanical performance at high temperatures [24]. Moreover, owing to the aromatic ring in the main chain of EP, it is mechanically stable under long-term irradiation [25]. Therefore, a new type of three functional epoxy resin AFG-90H was synthesized as the matrix of a neutron shielding material. Compared with ordinary EP, it has better neutron irradiation resistance, mechanical stability and thermal stability [26].

In order to improve the thermal neutron absorption performance of EP, it is important to select suitable neutron absorbers. The average macro-absorption cross-sections (Σ) of the neutron-absorbing elements Gd, B, Cd and Sm are 49,700, 3835, 2520 and 5922 barns at thermal neutron energy, respectively [27]. Figure 1 shows the absorption cross-sections of these four elements at different neutron energies. Gd has the highest thermal neutron capture cross-section among all of the stable nuclei. However, the neutron capture reaction for ^{157}Gd and ^{155}Gd emits a γ -ray cascade with a total energy of ~ 8 MeV [28]. B and its compounds (e.g., B_4C and BN) are good thermal neutron absorbers and are widely used in neutron shielding materials. Moreover, B compounds absorb neutrons through the reaction $^{10}B(n,\alpha)^7Li$ with the concomitant generation of helium bubbles [29]. Such helium bubbles cause the premature failure of materials. As is known, Cd is toxic, carcinogenic and harmful to human health and is not suitable to be used as a radiation protection element. It is usually used as an element in the Ag-In-Cd control rods of reactors [30].

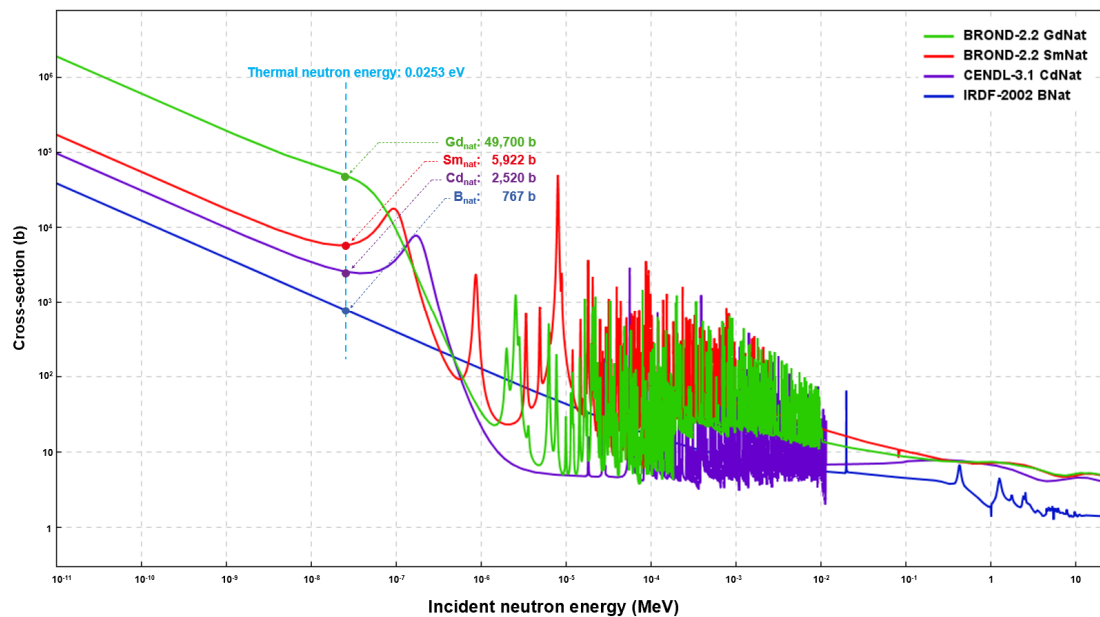


Figure 1. The neutron absorption cross-sections of Gd, B, Cd and Sm.

Samarium is found in many natural minerals, such as bastnaesite, monazite and samarskite [31]. The total reserve of Sm in the earth is approximately 2 million tons [32]. Sm is most commonly sold in the form of Sm_2O_3 , which is one of the cheapest rare earth oxides on the market (USD ~40/kg in China) [33]. Additionally, Sm is also a suitable neutron absorber; the natural abundance of ^{149}Sm is 13.9%, and most of its neutron capturing and decay products are also other isotopes of samarium [34]. Sm has a wider neutron absorption spectrum of 10^{-7} – 10^{-5} MeV compared to Gd and B. Therefore, it has the potential to be used as a neutron absorber for application in shielding materials.

The high content of fillers can cause their uneven distribution in the polymer matrix and poor interface interaction. This defect reduces the mechanical stability of EP composites. One issue is that high neutron shielding and mechanical performances cannot be well balanced. Generally, this is due to large differences in physicochemical properties between the inorganic filler and the epoxy resin matrix [35]. Constructing a chemical bond “bridge” is the key to strengthening interfacial interactions. This “bridge” can enable the orderly grafting of inorganic particles and organic molecular chains to improve the dispersion of fillers in the resin matrix [36]. Covalent modification is a simple fabrication method for particles. The silane coupling agent APTES contains two different chemical functional groups. One end of the functional group chain can react with silanol groups and then connect to the surface of inorganic materials such as glass fiber, silicate and metal oxide, etc. The other end can form covalent bonds with resin molecular chains. Thus, the coupling of the two incompatible materials can realize the equivalent function of a “bridge”.

In this work, Sm_2O_3 /AFG-90H composites were prepared by solution casting and ultrasonic mixing of epoxy resin matrix (AFG-90H) and surface-modified Sm_2O_3 . The Sm_2O_3 was used as the neutron absorber. Synchronous thermal analysis (TG-DSC) was used to analyze the thermal stability and glass transition temperature of the materials. The integrated neutron transport and safety evaluation software SuperMC [37] was used to analyze the neutron shielding performance of the materials coupled with the data library HENDL1.0 [38]. The microstructure and Fourier-transform infrared (FT-IR) spectroscopy of the Sm_2O_3 -APTES and Sm_2O_3 -APTES/AFG-90H were analyzed. The composites were characterized by X-ray diffraction (XRD). The influence of the mass fraction of fillers in the matrix on the mechanical properties of materials was studied.

2. Experimental

2.1. Materials

AFG-90H (Meisu Plastic Technology Co., Ltd., Shanghai, China.) was selected as the matrix, with 4,4'-diaminodiphenylsulfone (Yinsheng Chemicals Co., Ltd., Suzhou, China.) as the curing agent. Samarium oxide (Sm_2O_3 , purity 99.9%), liquid γ -aminopropyl triethoxysilane (APTES, 97%) and toluene (40%) were purchased from Runxiang Chemical Co., Ltd. (Changzhou, China) and Aladdin (Shanghai, China), respectively. Acetone and anhydrous ethanol were acquired from Sinopharm Chemical Reagent Co., Ltd. (Shanghai, China). Deionized water was produced by a Kertone labVIP (Hengqing Technology Co., Ltd., Hangzhou, China) machine and used in all experimental procedures. All chemical reagents and solvents were used as received. The molecular weight, density, crosslinking density, viscosity and epoxy equivalent of the AFG-90H resin are listed in Table 1.

Table 1. Basic properties of AFG-90H polymer.

Physical Properties	Value
Mw	556
Mn	317
Density (g/cm^3)	1.314
Cross-linking density	2179
Viscosity ($\text{mPa}\cdot\text{s}@25\text{ }^\circ\text{C}$)	1540
Epoxy equivalent (g/mol)	105

2.2. Surface Modification of Sm_2O_3 Powder

The silane coupling agent (APTES) was employed to modify the interfacial interaction of Sm_2O_3 particles. First, Sm_2O_3 particles were dispersed in 60 mL of toluene and stirred under nitrogen gas environment for 20 min before drying. This process was undertaken to clean the surface of the Sm_2O_3 particles. Secondly, Sm_2O_3 particles were ultrasonicated in 50 mL absolute ethanol for 40 min to form hydroxyl groups on the surface of the Sm_2O_3 particles. Absolute ethanol, deionized water and APTES were prepared as a solution with a volume ratio of 9:1:2.5. The glacial acetic acid was used to adjust the pH to 5. The hydrolyzed APTES solution was obtained after full stirring. Under mechanical stirring, the hydrolyzed APTES solution was added dropwise to the Sm_2O_3 suspension to react at room temperature for 24 h. After centrifuging the suspension, the particles were cleaned with absolute ethanol and acetone successively. Finally, the clean Sm_2O_3 powders were put into the oven and dried for 5 h. The surface modification procedure is shown in Figure 2a.

2.3. Fabrication of Sm_2O_3 -APTES/AFG-90H

To prepare Sm_2O_3 -APTES/AFG-90H composites, different contents of Sm_2O_3 -APTES (0–30 wt%) were dispersed into ethanol and ultrasonicated to form a uniform suspension. Subsequently, DDS and AFG-90H were configured into a pre-cured resin at a weight ratio of 5.58:10 and stirred in an oil bath at 105 °C to a low-viscosity state. Then, the dried Sm_2O_3 -APTES particles were poured into the resin solution under mechanical stirring and ultrasonically treated for 1 h to ensure that the Sm_2O_3 -APTES was evenly dispersed in the resin matrix. The mixed resin solution was dried at 80 °C to remove ethanol. Finally, the stirred mixture was poured into a Teflon mold and degassed at 90 °C to remove air bubbles. The Sm_2O_3 /AFG-90H composites was cured at 185 °C for 3 h and then removed from the mold. The diagram of the curing reaction is shown in Figure 2b.

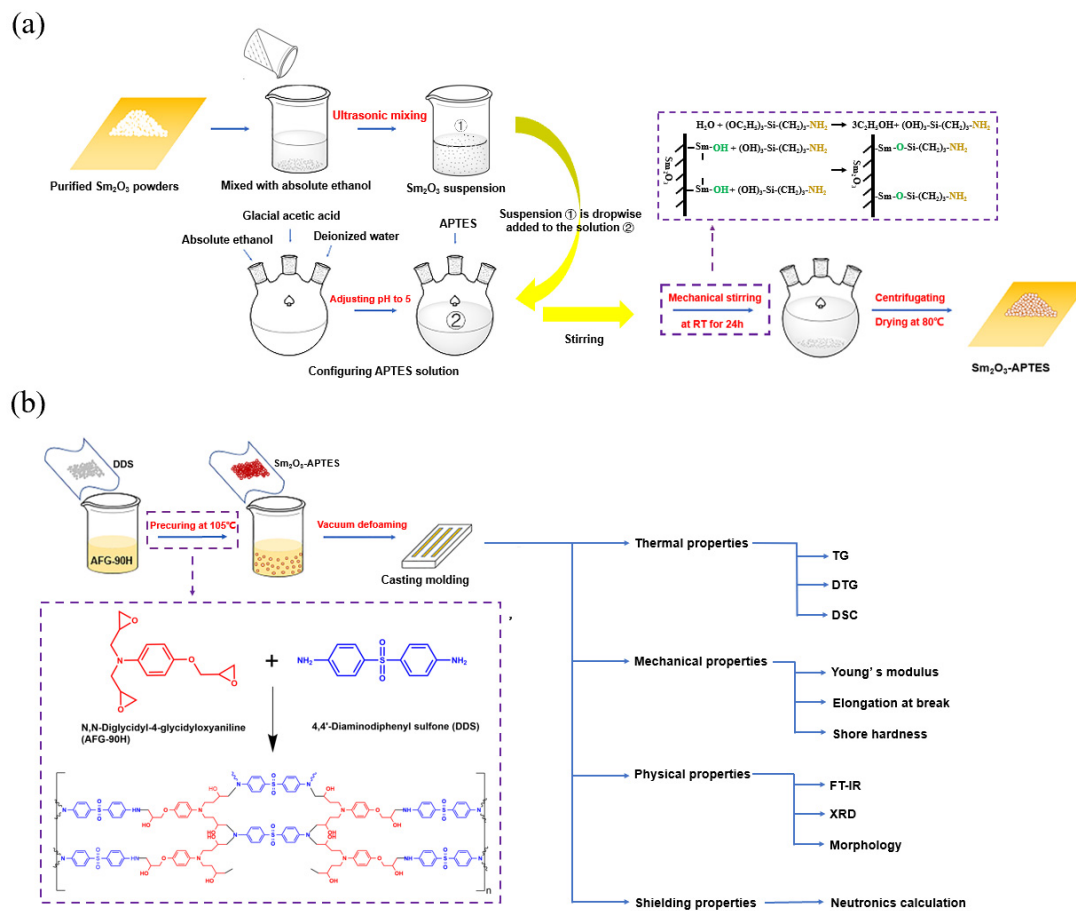


Figure 2. Schematic diagrams of modification process and curing progress: (a) scheme of the procedure for the preparation of Sm₂O₃-APTES; (b) diagram of curing reaction of *N,N*-diglycidyl-4-glycidyl-oxyaniline and 4,4'-aminodiphenyl sulfone.

2.4. Characterization Methods

Fourier transform infrared (FT-IR) spectra were measured using a Nicolet iS 10 spectrometer with the KBr squash technique and the test device was used to characterize the peaks of functional groups. X-ray diffraction (XRD) analyzed on the AFG-90H and Sm₂O₃ particles were performed on Rigaku Ultima IV X-ray diffractometer from 10° to 80°. Thermogravimetric analysis (TGA) and differential scanning calorimetry (DSC) were performed in an air atmosphere using a NETZSCH 449 F3 synchronous thermal analyzer under the heating rate of 10 °C/min. TG-DSC was used to analyze the thermal stability and glass transition temperature of Sm₂O₃-APTES/AFG-90H. Scanning electron microscopy (SEM, Carl Zeiss AG, Oberkochen, Germany) was performed to characterize the morphology of Sm₂O₃ particles and the surface of Sm₂O₃/AFG-90H composites, including its tensile cross-section of the tensile fracture test. Static mechanical testing was performed in accordance with ASTM D638-91 using an Instron 3369 Universal Testing Machine with a loading rate of 2 mm/min. At least four separate dumbbell-shaped samples were tested for each experiment. The Young's modulus (E) and elongation at break (e) of all samples were tested via the Instron 3369 machine. The Shore hardness of specimens was measured using a Shore D durometer in accordance with ASTM D2240 Shore hardness test method. The Shore hardness was measured five times at the surface with an interval of at least 6 mm for each sample and the average values were calculated.

3. Results and Discussion

3.1. Surface Modification of Sm₂O₃ Powders

The infrared spectra of APTES, Sm₂O₃ and Sm₂O₃-APTES are shown in Figure 3. As shown in the FT-IR spectrum of APTES, the absorption peak of the stretching vibration mode of O-H is 3419 cm⁻¹. The antisymmetric stretching vibration mode peaks of C-H are 2977 and 2927 cm⁻¹. Furthermore, the characteristic peaks of Si-O-C are 958 and 771 cm⁻¹. The in-plane bending vibration mode peaks of N-H are 1488 and 1567 cm⁻¹. The characteristic peaks of Si-O-Si and Si-O are 1116 and 1024 cm⁻¹ [39]. The Si-O-Si bond formed on the surface of non-Si-based materials was a weak chemical interaction formed between two APTES molecules [40]. When comparing the FTIR spectrums of APTES and Sm₂O₃-APTES, no obvious peaks were observed in the original Sm₂O₃ powders. In contrast, as shown in the FTIR spectrum of Sm₂O₃-APTES, all types of characteristic peaks of N-H at 1567 and 1488 cm⁻¹ were more prominent than in the APTES spectrum. This indicated that more Sm₂O₃-APTES particles were connected to each other through N-H bonds (as shown in Figure 4). In addition, the weak N-N characteristic peak can be seen at 1372 cm⁻¹. The FT-IR results indicate that the silane groups in APTES successfully formed covalent bonding with the surface of Sm₂O₃.

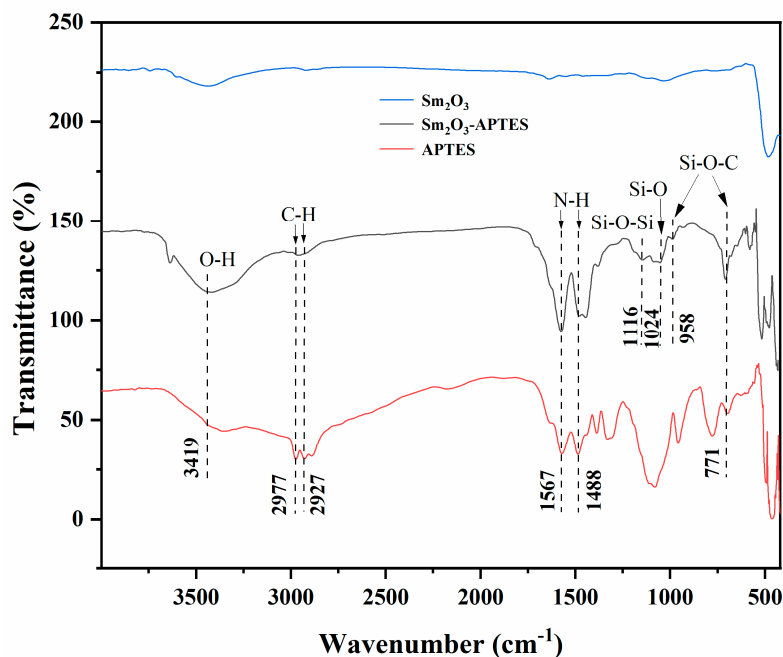


Figure 3. FT-IR spectra of APTES, Sm₂O₃ and Sm₂O₃-APTES.

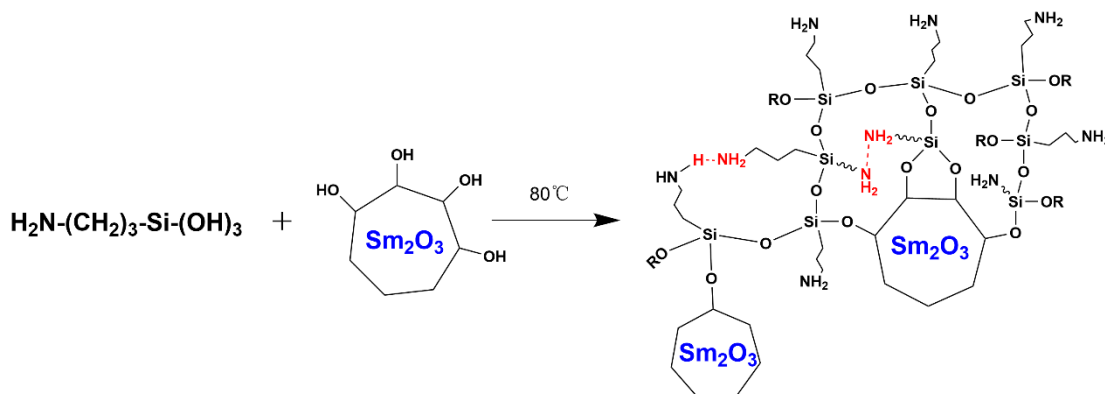


Figure 4. Functional mechanism of APTES on Sm₂O₃ powders.

3.2. XRD Patterns of Sm_2O_3 and Sm_2O_3 -APTES/AFG-90H Composites

The XRD diffraction patterns of Sm_2O_3 , Sm_2O_3 -APTES and Sm_2O_3 -APTES/AFG-90H are shown in Figure 5. The multimodal diffraction pattern of Sm_2O_3 showed that it belonged to the monoclinic crystal system. In addition, the Sm_2O_3 -APTES showed a similar trend as the original Sm_2O_3 , indicating that the crystal structures of Sm_2O_3 did not change during the surface modification process of APTES. Obviously, the existence of the characteristic signal of Sm_2O_3 at $2\theta = 25\text{--}65^\circ$ in the XRD pattern of Sm_2O_3 /AFG-90H composites confirmed the successful incorporation of Sm_2O_3 -APTES into the epoxy resin. The Sm_2O_3 -APTES/AFG-90H exhibits a broad hump at approximately 15° , indicating the amorphous properties of the matrix material [41].

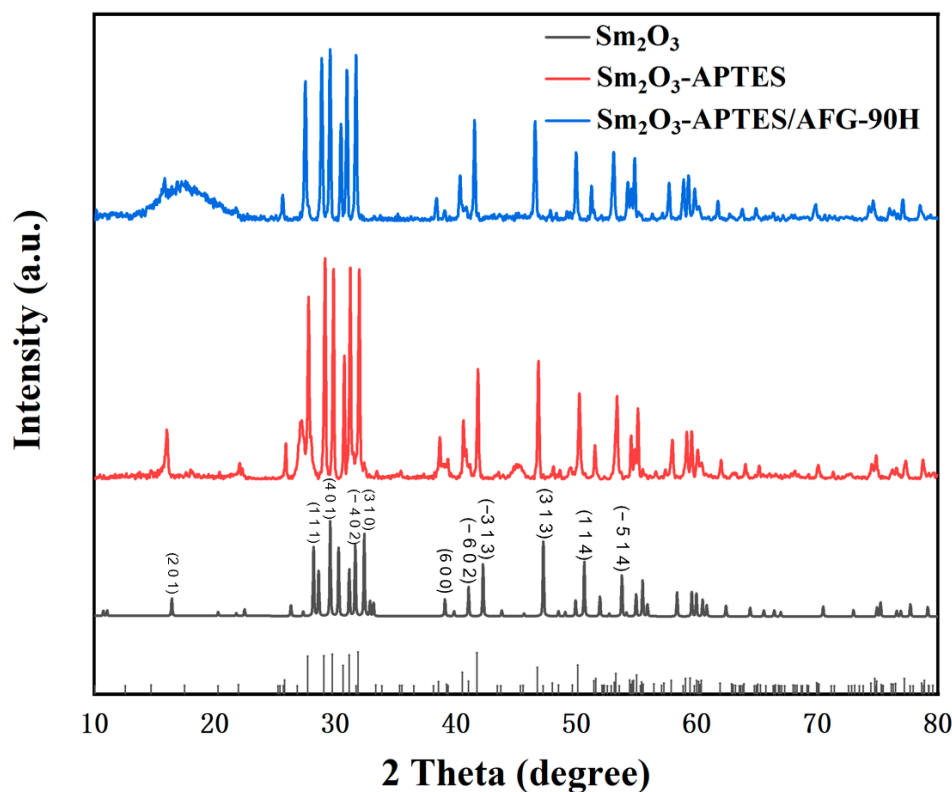


Figure 5. XRD patterns of Sm_2O_3 , Sm_2O_3 -APTES and Sm_2O_3 -APTES/AFG-90H.

3.3. Morphology Analysis

The morphology of the fractured surface of the Sm_2O_3 -APTES/AFG-90H composite was shown in Figure 6. The particles show an irregular polyhedron shape with fibrous protrusions and slight agglomeration (as shown in Figure 6a,b). The section of pure AFG-90H resin was smooth (as shown in Figure 6c,d). With the increase in Sm_2O_3 -APTES content, the fractured surface changed from smooth to rough. When the Sm_2O_3 -APTES content was less than 20 wt%, it was uniformly dispersed into the matrix resin and there were fewer interfacial voids (as shown in Figure 6e,f). At a content above 20 wt%, the particles began to agglomerate (as shown in Figure 6g,h) due to the increase in the probability of the interconnection of active free groups on the particle surface. Because the interfacial energy of the formation of aggregates between particles was less than the binding energy of particles and the matrix molecular chain, there was no obvious separation of aggregates from the matrix, indicating that the adhesion with the resin matrix was good, because the free radicals on the surface of the filler helped to strengthen the interfacial bonding energy between Sm_2O_3 -APTES and AFG-90H. However, when the Sm_2O_3 -APTES content was 30 wt%, an increase in the number of pores in the matrix was observed. Therefore, the extension of dispersion for the Sm_2O_3 -APTES particles in the matrix should be optimized

during the preparation process. In addition, the particle size distribution is shown in Figure 7. The average size of Sm_2O_3 -APTES was approximately $1.16 \mu\text{m}$. Sm_2O_3 -APTES particles of micrometer size can have a pinning effect on the epoxy resin matrix, which will be described in detail in Section 3.5.

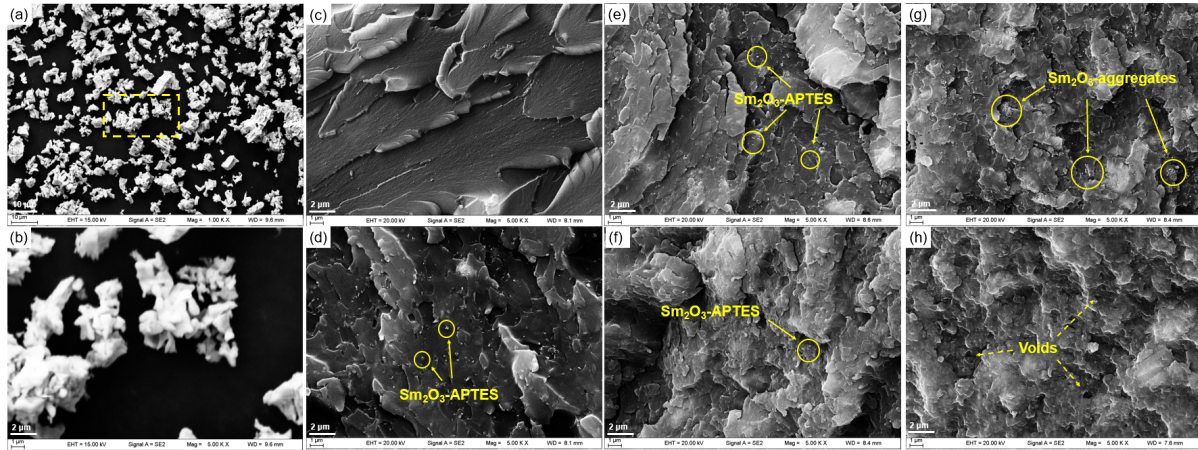


Figure 6. SEM images of Sm_2O_3 -APTES particles and morphology of Sm_2O_3 -APTES/AFG-90H: (a,b) Sm_2O_3 -APTES particles; (c–h) Sm_2O_3 -APTES content: 0, 5, 10, 15, 20, and 30 wt%.

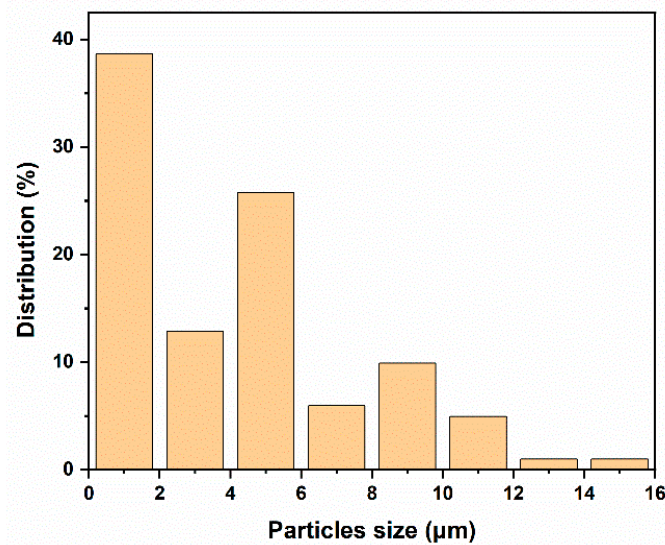


Figure 7. Size distribution of Sm_2O_3 -APTES powders.

3.4. Thermal Performance

The TG, DTG and DSC thermal analysis curves of Sm_2O_3 -APTES/AFG-90H are shown in Figure 8. The mass loss temperatures of the TG curve are listed in Table 2, where T_5 represents the temperature with a mass loss of 5 wt%, so for T_{10} , T_{50} and T_{max} .

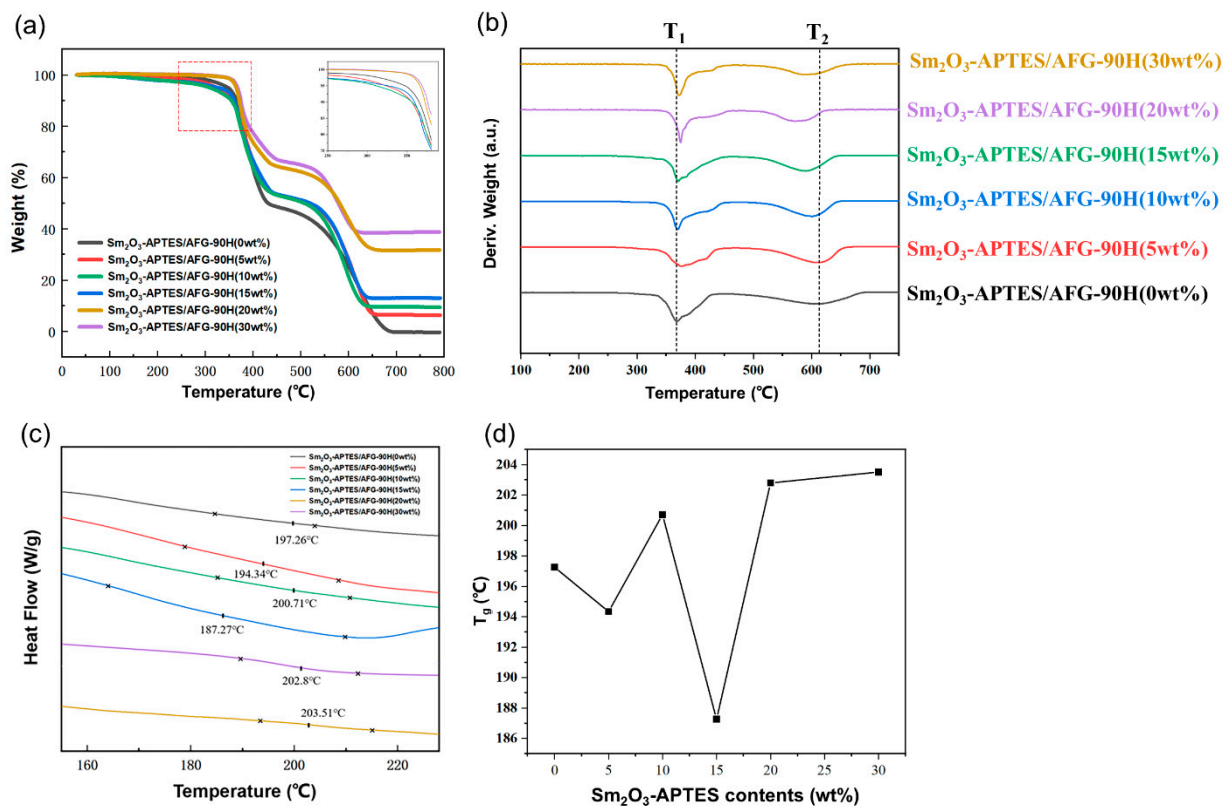


Figure 8. Thermal performance curves: (a) TG; (b) DTG; (c) DSC and (d) T_g of Sm₂O₃-APTES/AFG-90H.

Table 2. TG data for Sm₂O₃-APTES/AFG-90H (°C).

Sm ₂ O ₃ -APTES Content (wt%)	T ₅	T ₁₀	T ₅₀	T _{max}
0	347.7	361.4	431.5	693.7
5	325.2	357.1	514.4	659.9
10	309.6	354.5	506.7	644.9
15	327.3	360.8	519.7	646.2
20	364.5	371.1	581.3	662.4
30	367.5	374.4	578.3	623.7

As shown in Figure 8a, the two-stage decomposition process was found in all specimens, and these stages showed the conformation of the thermal decomposition trend for AFG-90H matrix. In the first stage, the thermal weight loss occurred at approximately 350 °C and the weight loss step continued to 430 °C. This decomposition reaction is attributed to the decomposition reaction of the epoxy network [42,43]. Owing to the existence of rigid structures (i.e., a benzene ring and an epoxy group) in the resin matrix, further decomposition of the composite was hindered. So, the curve remained flat in the temperature range from 430 to 530 °C [44]. In the second stage, the thermo-gravimetric range was from 530 to 650 °C. The polymer chain was completely decomposed and then the Sm₂O₃ was entirely separated from the matrix. The mass loss temperature was listed in Table 2, T₅ followed a downward trend when the Sm₂O₃-APTES content increased from 0 to 10 wt% and an upward trend when the content increased from 15 to 30 wt%, while the same was observed for T₁₀. When the Sm₂O₃-APTES content was 30 wt%, T₅ and T₁₀ increased by 5.4% and 3.6%, respectively, compared with that of the pure AFG-90H matrix. Microparticles increased physical crosslinking points and enhanced interfacial interactions. They play a positive role in inhibiting the initial decomposition [45].

The above results show that the agglomeration occurring with a high content of Sm₂O₃-APTES had a strong blocking effect on the thermal movement of the AFG-90H molecular chain, such as the weak chemical interaction between Sm₂O₃-APTES and AFG-90H. However, the maximum decomposition temperature T_{\max} of Sm₂O₃-APTES/AFG-90H decreased compared with that of pure AFG-90H. The decreased maximum decomposition temperature T_2 can also be seen in Figure 8b. In addition, T_g at the same heating rate as TG was calculated through the DSC curve (as shown in Figure 8c). The T_g of Sm₂O₃-APTES/AFG-90H with a low filler content (≤ 15 wt%) was irregular. This was due to the weak chemical force between the matrix molecular chains and Sm₂O₃-APTES with a low content. When the Sm₂O₃-APTES content was 30 wt%, T_g increased by 3.16% compared with that of pure AFG-90H.

The trend of T_g of Sm₂O₃-APTES/AFG-90H is shown in Figure 8d. Generally, T_g of polymer composites is affected by molecular weight, cross-linking density and particle-matrix interface area [46]. The trend of T_g vs. temperature could be due to the combined effects of two opposite factors [47]. On the one hand, the strong interfacial interaction between AFG-90H matrix and Sm₂O₃-APTES fillers could partially limit the motions of polymer chain segments and delay the occurrence of relaxation behavior at the glass transition region. This will reduce the flexibility of epoxy chain at high temperature and then lead to an increase in T_g . On the other hand, the addition of fillers could cause difficulty for the composites to achieve the same level of curing as the neat AFG-90H, and thus the cross-linking density decreases and leads to a decrease in T_g . In this work, when the content of Sm₂O₃-APTES is more than 20 wt%, the free volume of the resin decreases and the thermal movement of the chain end is limited by entangled Sm₂O₃-APTES agglomeration. Similar results can be found in Refs. [48,49]. The polymer chains need to absorb more energy to overcome the energy barrier, which leads to an increase in T_g . Conversely, T_g changes irregularly due to the interaction of the above two factors. Ref. [50] showed similar results on the polymer incorporated with APTES-modified particles.

3.5. Mechanical Properties of Sm₂O₃-APTES/AFG-90H

The mechanical properties of Sm₂O₃-APTES/AFG-90H are shown in Figure 9, including Young's modulus, elongation at break, tensile strength and Shore hardness. It is clear that the Young's modulus of Sm₂O₃-APTES/AFG-90H composites increased with an increase in Sm₂O₃-APTES content (as shown in Figure 9a). When the content of Sm₂O₃-APTES was 0–5 wt%, the Young's modulus increased slowly due to the good interfacial bonding between Sm₂O₃-APTES and the AFG-90H chains. When its content was 10–20 wt%, the Young's modulus growth increased faster with uniform dispersion of Sm₂O₃-APTES and good interface compatibility, which synergistically improves the modulus of composite materials. When its content was 30 wt%, the increased probability of Sm₂O₃ agglomeration could destroy the mechanical properties of the composite material, which was shown in Figure 9b. From the perspective of Shore hardness, the surface hardness of the material gradually increases with Sm₂O₃-APTES and finally reaches a saturation value (as shown in Figure 9c). The texture of the composite material is brittle and harder, indicating that Sm₂O₃-APTES can slightly increase the surface hardness of AFG-90H. Composite stiffness significantly depended on the Sm₂O₃-APTES particle content but not the particle/matrix adhesion, since the fillers had a much higher modulus than the matrix [51].

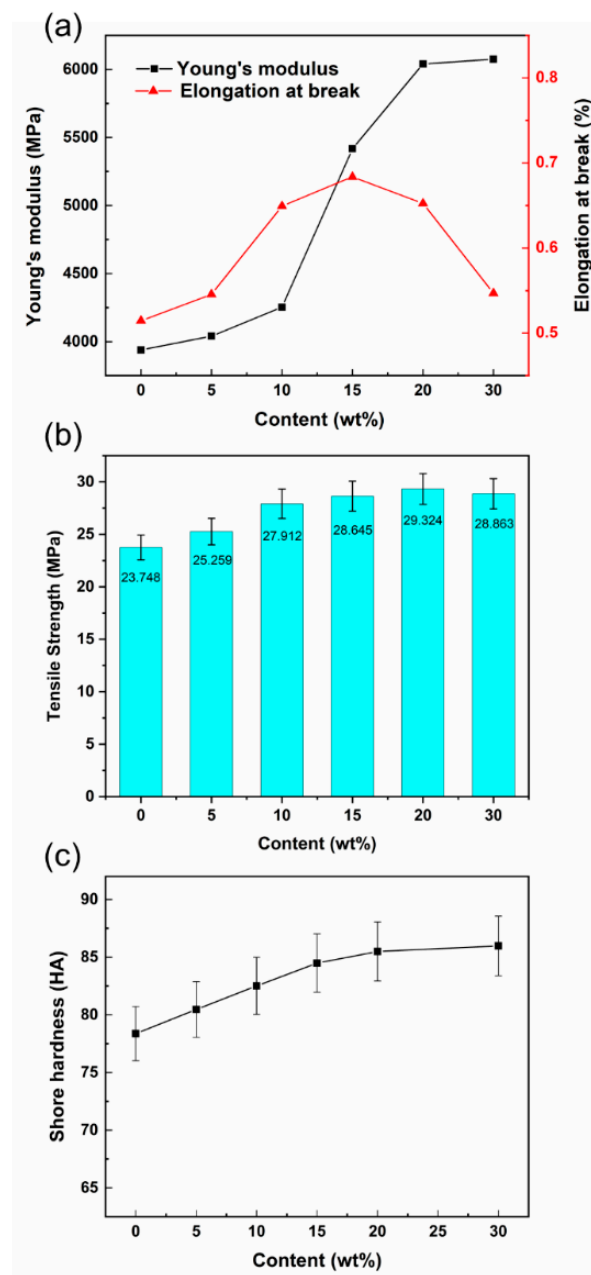


Figure 9. Mechanical properties of Sm₂O₃-APTES/AFG-90H: (a) Young's modulus and elongation at break; (b) tensile strength; (c) Shore hardness.

One criterion for judging the toughness of polymer materials is the elongation at break. The elongation at break of the composite reached a peak of 0.68%, and T_g was the lowest when the Sm₂O₃-APTES content was 15 wt% in this study. In order to further study the effect and mechanism of Sm₂O₃-APTES on the toughness of the composite material, the microscopic morphology of the tensile cross-section of the composite material was observed, as shown in Figure 10. When the Sm₂O₃-APTES content is 0–5 wt%, the fracture cross-section of the composites is neat and there is a single crack direction. Typical brittle fracture characteristics are shown in Figure 10a,b. When the content of Sm₂O₃-APTES is 5 wt%, a small amount is distributed in the AFG-90H matrix, which has little effect on the cracks and the good interface adhesion between Sm₂O₃-APTES and the matrix increases the material's toughness. When the content of Sm₂O₃-APTES is 10–15 wt%, the cracks are deflected, as shown by the yellow curve in Figure 10c,d, indicating that Sm₂O₃-APTES can be pinned in the matrix to prevent the cracks from propagating along the original direction

among the contents [52]. The delamination section appears because the stress gradually concentrates as the content increases. When its content is 20–30 wt%, agglomerates began to appear, the delamination phenomenon caused by stress concentration is more obvious and the compatibility of the agglomerated part and the matrix becomes poor. Therefore, part of the agglomerate comes out of the AFG-90H matrix when the tensile stress is loaded, causing holes and generating surrounding micro-cracks [53]. The rapid propagation of micro-cracks reduces the toughness of the matrix. The mechanism was analyzed based on the SEM images, and its diagram is shown in Figure 11. At a low Sm_2O_3 -APTES content (≤ 15 wt%), the crosslinking of particles and molecular chain can effectively disperse the stress. At a high Sm_2O_3 -APTES content (>15 wt%), the tensile stress of the matrix to the fillers is higher than its interfacial adhesion force. Therefore, the agglomerations have interfacial debonding and holes [54,55]. A large amount of local plastic deformation is exhibited around the equator of the particles. Hence, the overall fracture toughness is reduced.

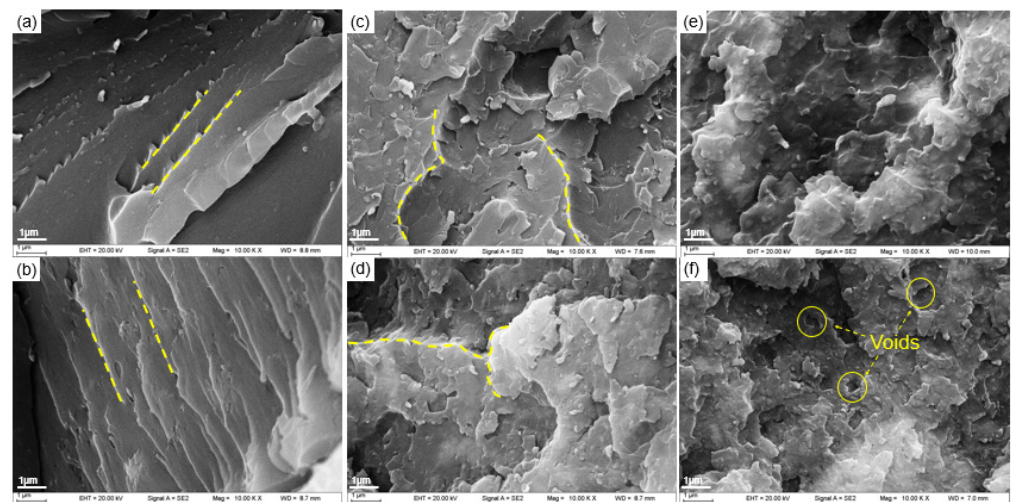


Figure 10. SEM images of tensile fracture surfaces for composites with different Sm_2O_3 -APTES contents: (a–f): 0, 5, 10, 15, 20 and 30 wt%.

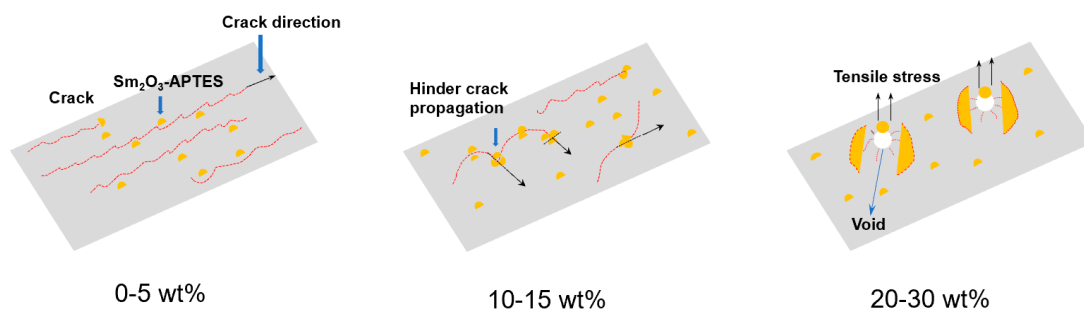


Figure 11. Mechanism diagram of Sm_2O_3 -APTES improving mechanical properties of composites.

3.6. Neutronics Simulation

Monte Carlo methods are widely used in nuclear engineering [56,57]. In this work, the neutron shielding performance of Sm_2O_3 /AFG-90H composite is simulated by the SuperMC software. The one-dimensional physical model adopted for the neutron shielding performance of the shielding material is shown in Figure 12. The simulation was performed in fixed neutron source mode. An isotropic thermal neutron point source with an average energy of 0.0253 eV was used and the fluence was 10^6 n/($\text{cm}^2 \cdot \text{s}$). The distance between the neutron source and the shielding material was 10 cm. The length perpendicular to the incident direction was defined as infinite, based on the assumption that all elements in the shielding material were uniformly dispersed. At least three measurements with

analog point neutron detectors were performed. The neutron shielding performance of the material was statistically evaluated by neutron permeability I/I_0 . The following equation was used for I/I_0 [58]:

$$\eta = I/I_0 = Ae^{-\Sigma d} + b$$

where η is the transmittance, I and I_0 are the intensities of the transmitted and incident neutron fluences (n/cm^2), A is the accumulation factor, d is the thickness of shielding material (cm), Σ is the total macro-cross-section (cm^{-1}) of all elements in the composite, and b is the background count. The secondary γ doses generated by the shielding material after capturing the thermal neutrons were recorded by the detector, and the flux was converted into dose through the dose conversion factor [59] to assess the level of gamma radiation. In addition, the Sm isotopic abundance and average thermal neutron absorption cross-section are listed in Table 3.

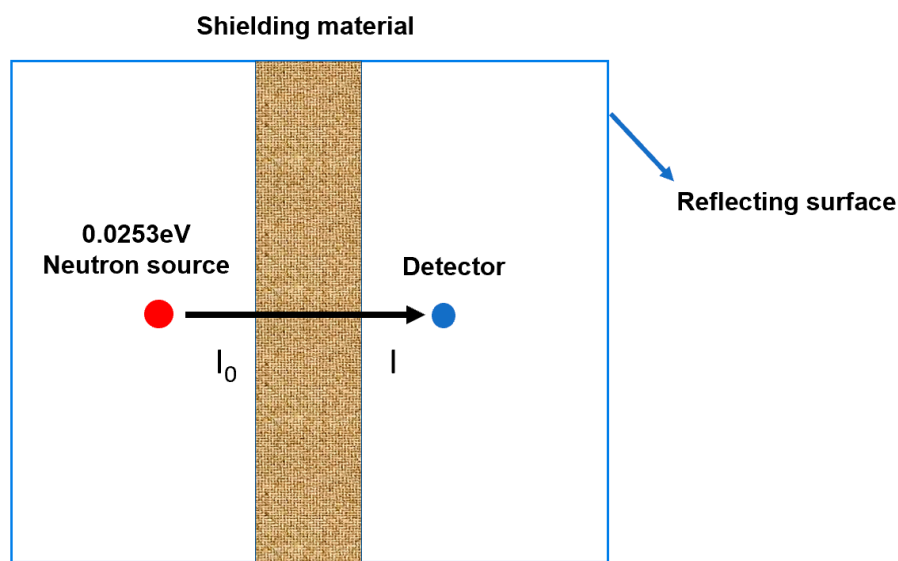


Figure 12. Schematic diagram of one-dimensional neutron shielding model.

Table 3. The isotopic composition and thermal neutron cross-section of natural samarium.

Isotope ^A Sm	Atomic Abundance (%)	σ_A (b)	$\sigma_{A,w}$ (b)
¹⁴⁴ Sm	3.1	0.7	0.02
¹⁴⁷ Sm	15.1	57	8.61
¹⁴⁸ Sm	11.3	2.4	0.27
¹⁴⁹ Sm	13.9	42,080	5849.12
¹⁵⁰ Sm	7.4	104	7.70
¹⁵² Sm	26.6	206	54.80
¹⁵⁴ Sm	22.6	8.4	1.90

The neutron shielding performance of Sm_2O_3 -APTES/AFG-90H is shown in Figure 13. It is clear that the value of the transmittance η decreased linearly with the increase in shielding material thickness and decreased with the increase in Sm_2O_3 -APTES content (as shown in Figure 13a), which indicated that the Sm element had good thermal neutron absorption performance. In the case of theoretical calculation, the η value for 30 wt% Sm_2O_3 -APTES/AFG-90H with a thickness of 0.2 cm is 98.86%, which is higher than that of the AFG-90H matrix. The secondary γ dose released by the shielding materials after absorbing thermal neutrons is shown in Figure 13b. The secondary γ dose produced by the composites after absorbing thermal neutrons was less than 10^{-14} Gy. With the increase in Sm_2O_3 content, the trend of the γ dose gradually transforms from a linear increase to a logarithmic increase. This indicates that the secondary γ dose generated by the composite

material absorbing thermal neutrons will reach a saturation value with the increasing content of Sm_2O_3 . The secondary γ at this dose level will be scattered in the environment without causing adverse damage to the human body or the environment.

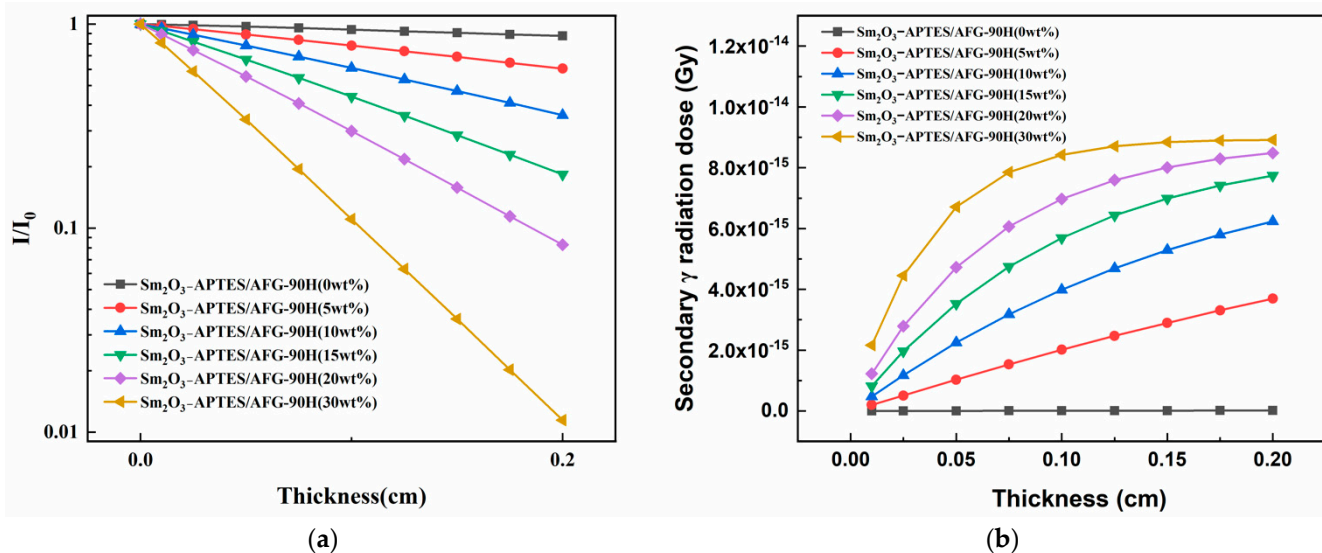


Figure 13. Shielding performance of Sm_2O_3 -APTES/AFG-90H: (a) neutron permeability (I/I_0); (b) secondary γ dose.

Moreover, Table 4 summarizes the physical properties of epoxy-based neutron shielding materials, including the decomposition temperatures of different mass loss, tensile strength and neutron permeability of different epoxy-based composites [60–62]. It shows that Sm_2O_3 -APTES/AFG-90H possessed better thermal stability and neutron shielding properties compared with other epoxy-based composites. The Sm_2O_3 -APTES/AFG-90H with 20–25 wt% Sm_2O_3 -APTES had good neutron shielding properties and the potential to be used as neutron shielding materials for advanced nuclear system.

Table 4. The decomposition temperature of different mass loss, tensile strength, neutron permeability of epoxy-based neutron shielding materials.

Shielding Materials	Decomposition Temperature ($^{\circ}\text{C}$)	Tensile Strength (MPa)	Neutron Permeability (%)	Reference No.
B_4C (5%)/epoxy resin	218 (5% mass loss)	32	56 (0.2 cm thickness)	[60]
Pb/B/GO /epoxy resin	332 (5% mass loss)	/	/	[61]
Gd (3%)/epoxy resin	342 (20% mass loss)	46	66 (0.5 cm thickness)	[62]
Sm_2O_3 -APTES (20%)/AFG-90H	364 (5% mass loss)	29	82 (0.2 cm thickness)	Our results

4. Conclusions

In this paper, a new type of high-performance epoxy resin AFG-90H and rare earth oxide Sm_2O_3 composites was prepared. The effects of Sm_2O_3 -APTES content on thermal properties, mechanical properties and neutron shielding properties were studied. The mechanism of its effect on mechanical properties was deeply studied. The main conclusions are as follows:

- (1) The uniform dispersion of Sm₂O₃ particles and good interface compatibility improved the strength and stiffness of Sm₂O₃-APTES/AFG-90H composites. When the Sm₂O₃-APTES content is 15 wt%, the composites have higher fracture toughness.
- (2) The Sm₂O₃-APTES hindered the thermal motion of molecular chains and improved the thermal stability of the composite at 340–380 °C. Simultaneously, the glass transition temperature T_g of the composites is slightly increased.
- (3) The shielding simulation showed that 30 wt% Sm₂O₃-APTES/AFG-90H had a higher neutron shielding performance than the AFG-90H matrix. After capturing neutrons, the secondary γ dose was 8.5×10^{-15} Gy.
- (4) The appropriate range of Sm₂O₃-APTES content in the epoxy matrix is 20–25 wt% to obtain higher properties.

In future work, the properties of Sm₂O₃-APTES/AFG-90H under neutron irradiation will be studied. The results indicate that the polymer composites have the potential for application in radiation protection.

Author Contributions: Conceptualization, Q.H. and H.W.; methodology, H.W., Q.H. and Y.Z.; software Q.H. and H.W.; validation, H.W., Q.H. and Y.Z.; formal analysis, H.W.; investigation, H.W. and Y.Z.; resources, Q.H. and Y.Z.; data curation, H.W.; writing—original draft preparation, H.W.; writing—review and editing, H.W., Q.H. and Y.Z.; visualization, H.W.; supervision, Q.H. and Y.Z.; project administration, Q.H.; funding acquisition, Q.H. and Y.Z. All authors have read and agreed to the published version of the manuscript.

Funding: This research was supported by the Key R&D Project of the Ministry of Science and Technology of China (with Grant No. 2020YFB1901900) and the project of “115” Industrial Innovation Team of Anhui Province.

Institutional Review Board Statement: Not applicable.

Informed Consent Statement: Not applicable.

Data Availability Statement: Not applicable.

Acknowledgments: We appreciate Chen Hu for the discussion on this work.

Conflicts of Interest: The authors declare no conflict of interest.

References

1. Abu-Khader, M.M. Recent advances in nuclear power: A review. *Prog. Nucl. Energy* **2009**, *51*, 225–235. [[CrossRef](#)]
2. Nambiar, S.; Yeow, J.T.W. Polymer-composite materials for radiation protection. *ACS Appl. Mater. Inter.* **2012**, *4*, 5717–5726. [[CrossRef](#)]
3. Korkut, T.; Gencel, O.; Kam, E.; Brostow, W. X-Ray, Gamma, and neutron radiation tests on epoxy-ferrochromium slag composites by experiments and Monte Carlo simulations. *Int. J. Polym. Anal. Charact.* **2013**, *18*, 224–231. [[CrossRef](#)]
4. More, C.V.; Alsayed, Z.; Badawi, M.S. Polymeric composite materials for radiation shielding: A review. *Environ. Chem. Lett.* **2021**, *19*, 2057–2090. [[CrossRef](#)]
5. Hu, C.; Huang, Q.; Zhai, Y. Thermal, mechanical investigation and neutron shielding analysis for Gd-MOF/polyimide materials. *RSC Adv.* **2021**, *11*, 40148–40158. [[CrossRef](#)]
6. Abdo, A.E.S.; Ali, M.A.M.; Ismail, M.R. Natural fiber high-density polyethylene and lead oxide composites for radiation shielding. *Radiat. Phys. Chem.* **2003**, *66*, 185–195. [[CrossRef](#)]
7. AbdelAziz, M.M.; Gwaily, S.E.; Makarious, A.S.; Abdo EI-Sayed, A. Ethylene-propylene diene rubber low density poly-ethylene boron carbide composites as neutron shields. *Polym. Degrad. Stab.* **1995**, *50*, 235–240. [[CrossRef](#)]
8. Karaevsky, S.K.; Potashev, S.I.; Drachev, A.I.; Burmistrov, Y.M. Data correction method for improving the spatial resolution of a position-sensitive ¹⁰B neutron detector. *Phys. At. Nucl.* **2019**, *82*, 1686–1689. [[CrossRef](#)]
9. Divya, M.; Albert, S.K.; Paul, V.T. Characterization of eutectic borides formed during solidification of borated stainless steel 304B4. *Weld. World* **2019**, *63*, 1681–1693. [[CrossRef](#)]
10. Maurya, P.; Maurya, P.; Sen, I.; Roy, S. A critical assessment of the processing parameters yielding an optimum combination of mechanical properties in cast Al-B₄C composites. *Trans. Indian Inst. Met.* **2021**, *74*, 1279–1294. [[CrossRef](#)]
11. Chidiac, S.E.; El-Samrah, M.G.; Reda, M.A. Mechanical and radiation shielding properties of concrete containing commercial boron carbide powder. *Constr. Build. Mater.* **2021**, *313*, 125466. [[CrossRef](#)]
12. Sevim, U.K.; Lumen, Y. Strength and fresh properties of borogypsum concrete. *Constr. Build. Mater.* **2013**, *48*, 342–347. [[CrossRef](#)]

13. Shin, J.W.; Lee, J.W.; Yu, S.; Baek, B.K.; Hong, J.P.; Seo, Y.; Kim, W.N.; Hong, S.M.; Koo, C.M. Polyethylene/boron-containing composites for radiation shielding. *Thermochim. Acta* **2014**, *585*, 5–9. [[CrossRef](#)]
14. Uddin, Z.; Yasin, T.; Shafiq, M.; Raza, A.; Zahur, A. On the physical, chemical and neutron shielding properties of polyethylene/boron carbide composites. *Radiat. Phys. Chem.* **2020**, *166*, 108450. [[CrossRef](#)]
15. Abdulrahman, S.T.; Ahmad, Z.; Thomas, S.; Maria, H.J.; Rahman, A.A. Viscoelastic and thermal properties of natural rubber low-density polyethylene composites with boric acid and borax. *J. Appl. Polym. Sci.* **2020**, *137*, e49372. [[CrossRef](#)]
16. Shang, Y.; Yang, G.; Su, F.; Feng, Y.Z.; Ji, X.Y.; Liu, D.; Yin, R.; Liu, C.T.; Shen, C.Y. Multilayer polyethylene/ hexagonal boron nitride composites showing high neutron shielding efficiency and thermal conductivity. *Compos. Commun.* **2020**, *19*, 147–153. [[CrossRef](#)]
17. Sayyed, M.I.; Abdalsalam, A.H.; Taki, M.M.; Mhareb, M.H.A.; Alim, B.; Baltakesmez, A.; Sakar, E. MoO₃ reinforced ultra-high molecular weight PE for neutrons shielding applications. *Radiat. Phys. Chem.* **2020**, *172*, 108852. [[CrossRef](#)]
18. Hu, C.; Zhai, Y.T.; Song, L.L.; Mao, X.D. Structure-thermal activity relationship in a novel polymer/MOF-based neutron-shielding material. *Polym. Compos.* **2020**, *41*, 1418–1427. [[CrossRef](#)]
19. Aygun, B.; Korkut, T.; Karabulut, A.; Gencel, O.; Karabulut, A. Production and neutron irradiation tests on a new epoxy/molybdenum composite. *Int. J. Polym. Anal. Charact.* **2015**, *20*, 323–329. [[CrossRef](#)]
20. Güngör, A.; Akbay, I.K.; Özdemir, T. EPDM rubber with hexagonal boron nitride: A thermal neutron shielding composite. *Radiat. Phys. Chem.* **2019**, *165*, 108391. [[CrossRef](#)]
21. Baykara, O.; İrim, S.G.; Wis, A.A.; Keskin, M.A.; Ozkoc, G.; Avc, A.; Dogru, M. Polyimide nanocomposites in ternary structure: A novel simultaneous neutron and gamma-ray shielding material. *Polym. Adv. Technol.* **2020**, *31*, 2466–2479. [[CrossRef](#)]
22. Li, X.M.; Wu, J.Y.; Tang, C.Y.; He, Z.K.; Yuan, P.; Sun, Y.; Lau, W.M.; Zhang, K.; Mei, J.; Huang, Y.H. High temperature resistant polyimide/boron carbide composites for neutron radiation shielding. *Compos. Part B-Eng.* **2019**, *159*, 355–361. [[CrossRef](#)]
23. Wu, Y.; Chen, G.; Zhan, M.; Yang, J. High heat resistant carbon fiber/polyimide composites with neutron shielding performance. *Prog. Org. Coat.* **2019**, *132*, 184–190. [[CrossRef](#)]
24. Jiang, Y.F.; Luan, W.; Zhang, X.; Han, Y.L.; Sun, K. Preparation of AFG-90H epoxy resin-based temperature-resistant neutron shielding composite. *Nucl. Tech.* **2015**, *38*, 120202.
25. Adeli, R.; Shirmardi, S.P.; Ahmadi, S.J. Neutron irradiation tests on B₄C/epoxy composite for neutron shielding application and the parameters assay. *Radiat. Phys. Chem.* **2016**, *127*, 140–146. [[CrossRef](#)]
26. Okuno, K. Neutron shielding material based on colemanite and epoxy resin. *Radiat. Prot. Dosim.* **2005**, *115*, 258–261. [[CrossRef](#)]
27. Talamo, A.; Gudowski, W. Comparative studies of JENDL-3.3, JENDL-3.2, JEFF-3, JEF-2.2 AND ENDF/B-6.8 data libraries on the Monte Carlo continuous energy modeling of the gas turbine-modular helium reactor operating with thorium fuels. *J. Nucl. Sci. Technol.* **2005**, *42*, 1040–1053. [[CrossRef](#)]
28. Dumazert, J.; Coulon, R.; Lecomte, Q.; Bertrand, G.H.V.; Hamel, M. Gadolinium for neutron detection in current nuclear instrumentation research: A review. *Nucl. Instrum. Methods A* **2018**, *882*, 53–68. [[CrossRef](#)]
29. Allen, T.; Busby, J.; Meyer, M.; Petti, D. Materials challenges for nuclear systems. *Mater. Today* **2010**, *13*, 14–23. [[CrossRef](#)]
30. Muhammad, F. Effects of high density dispersion fuel loading on the control rod worth of a low enriched uranium fueled material test research reactor. *Ann. Nucl. Energy* **2013**, *58*, 19–24. [[CrossRef](#)]
31. Lucas, J.; Lucas, P.; le Mercier, T.; Rollat, A.; Davenport, W. *Rare Earths*; Elsevier: Amsterdam, The Netherlands, 2015; p. 370.
32. Harris, J. *Nature's Building Blocks: An A-Z Guide to the Elements*; Maney Publishing: Leeds, UK, 2002; p. 932.
33. Fernandez, V. Rare-earth elements market: A historical and financial perspective. *Resour. Policy* **2017**, *53*, 26–45. [[CrossRef](#)]
34. Florez, R.; Colorado, H.A.; Giraldo, C.H.C.; Alajo, A. Preparation and characterization of Portland cement pastes with Sm₂O₃ microparticle additions for neutron shielding applications. *Constr. Build. Mater.* **2018**, *191*, 498–506. [[CrossRef](#)]
35. Chen, R.C.; Zhang, Q.P.; Ke, K.; Sun, N.; Xu, W.D.; Liu, D.L.; Yang, W.B.; Li, Y.T.; Zhou, Y.L.; Yang, M.B.; et al. Chemically bonding BaTiO₃ nanoparticles in highly filled polymer nanocomposites for greatly enhanced dielectric properties. *J. Mater. Chem. C* **2020**, *8*, 8786–8795. [[CrossRef](#)]
36. Zhu, S.; Qian, Y.; Hassan, E.A.M.; Shi, R.J.; Yang, L.L.; Cao, H.J.; Zhou, J.F.; Ge, D.T.; Yu, M.H. Enhanced interfacial interactions by PEEK-grafting and coupling of acylated CNT for GF/PEEK composites. *Compos. Commun.* **2020**, *18*, 43–48. [[CrossRef](#)]
37. Wu, Y.C.; Song, J.; Zheng, H.Q. CAD-based Monte Carlo program for integrated simulation of nuclear system SuperMC. *Ann. Nucl. Energy* **2015**, *82*, 161–168. [[CrossRef](#)]
38. Xu, D.Z.; Gao, C.J.; Wu, Y.C. Development on hybrid evaluated nuclear data library HENDL1.0/MG/MC. *Nucl. Phys. Rev.* **2004**, *21*, 415–418.
39. Zhi, X.; Mao, Y.Y.; Yu, Z.Z. γ -Aminopropyl triethoxysilane functionalized graphene oxide for composites with high dielectric constant and low dielectric loss. *Compos. Part A-Appl. Sci.* **2015**, *76*, 194–202. [[CrossRef](#)]
40. Meroni, D.; Lo Presti, L.; Di Liberto, G. A close look at the structure of the tio2-aptres interface in hybrid nanomaterials and its degradation pathway: An experimental and theoretical study. *Langmuir* **2017**, *121*, 430–440. [[CrossRef](#)]
41. Goyat, M.S.; Rana, S.; Halder, S.; Ghosh, P.K. Facile fabrication of epoxy-TiO₂ nanocomposites: A critical analysis of TiO₂ impact on mechanical properties and toughening mechanisms. *Ultrason. Sonochemistry* **2018**, *40*, 861–873. [[CrossRef](#)]
42. Duan, J.K.; Kim, C.N.; Jiang, P.K. On-line monitoring of cycloaliphatic epoxy/acrylate interpenetrating polymer networks formation and characterization of their mechanical properties. *J. Polym. Res.* **2009**, *16*, 45–54. [[CrossRef](#)]

43. Duan, J.K.; Kim, C.N.; Yun, Z.; Jiang, P.K. Morphology and thermal and dielectric behavior of cycloaliphatic epoxy/trimethacrylate interpenetrating polymer networks for vacuum-pressure-impregnation electrical insulation. *J. Appl. Polym. Sci.* **2008**, *110*, 3096–3106. [[CrossRef](#)]
44. Mahdi, E.M.; Tan, J.C. Dynamic molecular interactions between polyurethane and ZIF-8 in a polymer-MOF nanocomposite: Microstructural, thermo-mechanical and viscoelastic effects. *Polymer* **2016**, *97*, 31–43. [[CrossRef](#)]
45. Permal, A.; Devarajan, M.; Huong, L.H.; Zahner, T.; Lacey, D.; Ibrahim, K. Enhanced thermal and mechanical properties of epoxy composites filled with hybrid filler system of aluminium nitride and boron nitride. *Polym. Compos.* **2018**, *39*, E1372–E1380. [[CrossRef](#)]
46. Sun, Y.Y.; Zhang, Z.Q.; Moon, K.S.; Wong, C.P. Glass transition and relaxation behavior of epoxy nanocomposites. *J. Polym. Sci. Pol. Phys.* **2004**, *21*, 3849–3858. [[CrossRef](#)]
47. Hou, J.; Li, G.H.; Yang, N.; Qin, L.L.; Grami, M.E.; Zhang, Q.X.; Wang, N.Y.; Qu, X.W. Preparation and characterization of surface modified boron nitride epoxy composites with enhanced thermal conductivity. *RSC Adv.* **2014**, *4*, 44282–44290. [[CrossRef](#)]
48. Liang, Z.M.; Yin, J.; Wu, J.H.; He, F.F. Polyimide/montmorillonite nanocomposites with photolithographic properties. *Eur. Polym. J.* **2004**, *40*, 307–314. [[CrossRef](#)]
49. Zhu, S.Y.; Zhang, X.M.; Chen, W.X.; Feng, L.F. Synthesis, characterization, and properties of polystyrene/SiO₂ hybrid materials via sol-gel process. *Polym. Compos.* **2015**, *36*, 482–488. [[CrossRef](#)]
50. Ma, S.Q.; Liu, W.Q.; Li, H.J. Morphologies and mechanical and thermal properties of epoxy resins modified by a novel polysiloxane capped with silane coupling agent, epoxide, and imino groups. *J. Macromol. Sci. Part B* **2011**, *50*, 975–987. [[CrossRef](#)]
51. Fu, S.Y.; Feng, X.Q.; Lauke, B.; Mai, Y.W. Effects of particle size, particle/matrix interface adhesion and particle loading on mechanical properties of particulate-polymer composites. *Compos. Part B-Eng.* **2004**, *42*, 3849–3858. [[CrossRef](#)]
52. Zaman, I.; Kuan, H.C.; Dai, J.F.; Kawashima, N.; Michelmore, A.; Sovi, A.; Dong, S.Y.; Luong, L.; Ma, J. From carbon nanotubes and silicate layers to graphene platelets for polymer nanocomposites. *Nanoscale* **2012**, *4*, 4578–4586. [[CrossRef](#)]
53. Chisholm, N.; Mahfuz, H.; Rangari, V.K. Fabrication and mechanical characterization of carbon/SiC-epoxy nanocomposites. *Compos. Struct.* **2005**, *67*, 115–124. [[CrossRef](#)]
54. Rubab, Z.; Afzal, A.; Siddiqi, H.M.; Saeed, S. Preparation, Characterization, and Enhanced Thermal and Mechanical Properties of Epoxy-Titania Composites. *Sci. World J.* **2014**, 515739. [[CrossRef](#)] [[PubMed](#)]
55. Wazzan, A.A.; Al-Turaif, H.A.; Abdelkader, A.F. Influence of submicron TiO₂ particles on the mechanical properties and fracture characteristics of cured epoxy resin. *Polym. Plast. Technol.* **2006**, *45*, 1155–1161. [[CrossRef](#)]
56. Lemaire, S.; Talou, P.; Kawano, T.; Chadwick, M.B.; Madland, D.G. Monte Carlo approach to sequential neutron emission from fission fragments. *Phys. Rev. C* **2005**, *72*, 024601. [[CrossRef](#)]
57. Nollett, K.M.; Pieper, S.C.; Wiringa, R.B.; Carlson, J.; Hale, G.M. Quantum Monte Carlo calculations of neutron- α scattering. *Phys. Rev. Lett.* **2007**, *99*, 022502. [[CrossRef](#)] [[PubMed](#)]
58. Wang, P.; Tang, X.; Chai, H.; Chen, D.; Qiu, Y.L. Design, fabrication and properties of a continuous carbon-fiber reinforced Sm₂O₃/polyimide gamma ray/neutron shielding material. *Fusion Eng. Des.* **2015**, *101*, 218–255. [[CrossRef](#)]
59. Sanusi, M.S.M.; Hassan, W.M.S.W.; Hashim, S.; Ramli, A.T. Tabulation of organ dose conversion factors for terrestrial radioactivity monitoring program. *Appl. Radiat. Isot.* **2021**, *174*, 109791. [[CrossRef](#)]
60. Kiani, M.A.; Ahmadi, S.J.; Outokesh, M.; Adeli, R.; Mohamnadi, A. Preparation and characteristics of epoxy/clay/B₄C nanocomposite at high concentration of boron carbide for neutron shielding application. *Radiat. Phys. Chem.* **2017**, *141*, 223–228. [[CrossRef](#)]
61. Hu, G.; Shi, G.; Hu, H.S.; Yang, Q.Z.; Yu, B.; Sun, W.Q. Development of gradient composite shielding material for shielding neutrons and gamma rays. *Nucl. Eng. Technol.* **2020**, *52*, 2387–2393. [[CrossRef](#)]
62. Galehdari, N.A.; Kelkar, A.D. Effect of neutron radiation on the mechanical and thermophysical properties of nanoengineered polymer composites. *J. Mater. Res.* **2017**, *141*, 223–228. [[CrossRef](#)]